Manifestation of a topological gapless phase in a two-dimensional chiral symmetric system through Loschmidt echo

K. L. Zhang and Z. Song[*]

School of Physics, Nankai University, Tianjin 300071, China

Unlike the edge state of a topological insulator where its energy level lives in the bulk energy gap, the edge state of a topological semimetal hides in the bulk spectrum and is difficult to be identified by the energy. We investigate the sensitivity of bulk and edge states of the gapless phase for a topological semimetal to the disordered perturbation via a concrete two-dimensional chiral symmetric lattice model. The topological gapless phase is characterized by two opposite vortices in the momentum space and nonzero winding numbers, which correspond to the edge flatband when the open boundary condition is applied. For this system, numerical results reveal that a distinguishing feature is that the robustness of the edge states against weak disorder and the flatband edge modes remain locked at zero energy in the presence of weak chiral-symmetry-preserving disorder. We employ the Loschmidt echo (LE) for both bulk and edge states to study the dynamic effect of disordered perturbation. We show that, for an initial bulk state, the LE decays exponentially, whereas it converges to a constant for an initial edge state in the presence of weak disorder. Furthermore, the convergent LE can be utilized to identify the positions of vortices as well as the phase diagram. We discuss the realization of such dynamic investigations in a topological photonic system.

I. INTRODUCTION

Topological states of matter [1–4] have become the focus of intense research in many branches of physics and provide a fertile ground for demonstrating the concepts in high-energy physics, including Majorana [5–10], Dirac [11–17], and Weyl fermions [18–26]. These concepts relate to topological gapless phases and corresponding edge modes not only exhibiting new physical phenomena with potential technological applications, but also deepening our understanding on state of matters. The system in the topological gapless phase exhibits band structures with band-touching points in the momentum space where these kinds of nodal points appear as topological defects of the Bloch vector field. On the other hand, a gapped phase can be topologically nontrivial, commonly referred to as topological insulators and superconductors. Such a phase is associated, at least, with two isolated bulk energy bands where the band structure of each is characterized by nontrivial topological index. A particularly important concept is the bulk-boundary correspondence, which links the nontrivial topological invariant in the bulk to the localized edge modes. In general, edge states are the eigenstates of Hamiltonian that are exponentially localized at the boundary of the system. A gapped topological phase is always associated with a bulk energy gap, whereas a topological gapless phase, commonly referred to as topological semimetals and nodal superconductors, can exhibit topological protected Fermi points or nodal points (we refer to the bulk energy gap as the energy gap of the system with translational symmetry and without disorder

throughout this paper). Accordingly, unlike the edge state of a topological insulator where its energy level lives in the bulk energy gap, the edge state of a topological gapless phase hides in the bulk spectrum, and is hard to be identified by the energy. These edge states can form a partial flatband in a ribbon geometry [27–29], which also exhibit robustness against disorder [30]. Recently, it has been pointed that Majorana zero modes are not only attributed to topological superconductors. A two-dimensional (2D) topologically trivial superconductors without chiral edge modes can host robust Majorana zero modes in topological defects [31–33]. In an experimental aspect, photonic systems provide a convenient and versatile platform to design various topological lattice models and study different topological states [34,35].

In this paper, we investigate the sensitivity of bulk and edge states of the gapless phase for a topological semimetal to the disordered perturbation via a concrete two-dimensional chiral symmetric lattice model. We employ the Loschmidt echo (LE) for both bulk and edge states to study the dynamic effect of disordered perturbation. The LE is a measure of the revival occurring when an imperfect time-reversal procedure is applied to a complex quantum system. It allows to quantify the sensitivity of quantum evolution to perturbations. This paper aims to shed light on the nature of topological edge modes associated with the gapless phase for a topological semimetal with chiral symmetry rather than gapped topological materials. We show that, for a initial bulk state, LE decays exponentially, whereas it converges to a constant for an initial edge state in the presence of weak chiral-symmetry-preserving disorder. Our results provide a dynamic way to identify topological edge states arising from the topological gapless phase in a 2D chiral symmetric system. The reason

is that unlike the edge states in a topological insulator, here, the edge flatband hides in a continuous spectrum. There is no bulk energy gap to protect the channel of the edge states. Thanks to the photonic system where the Pauli exclusion is not obeyed, a single-particle state can be amplified by the large population of photons. The phase diagram can be detected by using edge-state photon dynamics.

This paper is organized as follows. In Sec. II, we present the introduction of the Loschmidt echo and the idea about applying it to the bulk and edge states in gapless systems. In Sec. III, we introduce a square lattice without disorder to illustrate our method. Section IV focuses on the dynamics of the system in the presence of disorder and demonstrates the dynamics method for detecting edge modes. Finally, our conclusion and discussion are given in Sec. V.

II. EDGE STATES AND LOSCHMIDT ECHO

Anderson localization is a basic condensed-matter physics phenomenon, which describes the absence of diffusion of waves in a disordered medium [36]. It turns out that particle localization is possible in a lattice potential, provided that the strength of disorder in the lattice is sufficiently large. The confinement of waves in a disordered medium has been observed for electromagnetic [37,38] and acoustic [39] waves in disordered dielectric structures and for electron waves in condensed matter. On the other hand, to capture the effect of disorder on the dynamics, one can employ a concept of the LE or fidelity. The LE is a measure of reversibility and sensitivity to perturbations of quantum evolutions. An initial quantum state $|\psi(0)\rangle$ evolves during a time T under a Hamiltonian H_0 reaching state $|\psi(t)\rangle$. Aiming to recover initial-state $|\psi(0)\rangle$, a new Hamiltonian H is applied between T and $2T$. Quantity $|\langle\psi(0)|e^{-iHt}e^{-iH_0t}|\psi(0)\rangle|^2$ is induced to measure the fidelity of this recovery. Perfect recovery of $|\psi(0)\rangle$ would be achieved by choosing $H = -H_0$. In the context of the present paper, the LE is defined as

$$M(t) = |\langle\psi(0)|e^{iH_{\mathrm{D}}t}e^{-iH_0t}|\psi(0)\rangle|^2, \qquad (1)$$

where $|\psi(0)\rangle$ is the state of the system at time $t = 0$, H_0 is the Hamiltonian of a uniform system, H_{D} is the Hamiltonian H_0 under disordered perturbation. For certain topological non-trivial systems, edge states are robust under a weak symmetry-preserving disorder, still being the localized state [34,40,41]. Particularly, we numerically observe that the corresponding eigenenergy is locked at zero as it is shown through a concrete model in Sec. IV. Therefore, considering such a topological system, it is expected that: (i) When an initial quantum state $|\psi(0)\rangle$ is a local state at bulk, $M(t)$ could decay to zero due to the fact that $e^{-iH_0t}|\psi(0)\rangle$ and $e^{-iH_{\mathrm{D}}t}|\psi(0)\rangle$ diffuse in 2D space in different ways, (ii) when $|\psi(0)\rangle$ is an edge state of H_0, $M(t)$ could be the constant 1.

Here, we consider the LE for a local state $|\psi(0)\rangle$ at the edges. We note that $|\psi(0)\rangle$ is almost written as the superposition of the flatband edge modes of H_0 or H_{D}, respectively, which result in

$$H_0|\psi(0)\rangle \approx 0, \quad H_{\mathrm{D}}|\psi(0)\rangle \approx 0 \qquad (2)$$

for weak disordered perturbation $H_{\mathrm{D}} - H_0 \ll H_0$. Then, we always have

$$\begin{aligned} M(t) &= |\langle\psi(0)|e^{iH_{\mathrm{D}}t}e^{-iH_0t}|\psi(0)\rangle|^2 \\ &\approx |\langle\psi(0)|\psi(0)\rangle|^2 \\ &= 1. \end{aligned} \qquad (3)$$

In the following, we will demonstrate this analysis through a concrete example.

III. MODEL WITHOUT DISORDER

We focus on a concrete 2D chiral symmetric model to demonstrate the main idea. In the previous works [42,43], we have demonstrated that a topologically trivial superconductor emerges as a topological gapless state, which support Majorana flatband edge modes. The quantum state is characterized by two band-degeneracy points with opposite chirality. In the present paper, we directly consider a tight-binding model with the same structure as the Majorana lattice. In the following: (i) We present the Hamiltonian and the phase diagram for the topological gapless phase; (ii) we investigate the topological edge states with nonzero winding numbers.

A. Model and topological gapless phase

We consider a tight-binding model on a bipartite $M \times N$ lattice with the Hamiltonian,

$$H = \sum_{\mathbf{r}}(\mu a_{\mathbf{r}}^{\dagger}b_{\mathbf{r}} + a_{\mathbf{r}}^{\dagger}b_{\mathbf{r}+\hat{x}} + a_{\mathbf{r}}^{\dagger}b_{\mathbf{r}+\hat{y}}) + \mathrm{H.c.}, \qquad (4)$$

where $\mathbf{r} = (j, l)$ is the coordinate of the lattice sites and $a_{\mathbf{r}}$ and $b_{\mathbf{r}}$ are the fermion or boson annihilation operators at site $\mathbf{r}$ in the sublattice of A and B, respectively. Vectors $\hat{x}$, $\hat{y}$ are the unitary lattice vectors in the x and y directions. The hopping between neighboring sites is described by the hopping amplitudes μ and 1. The schematic for the honeycomb lattice is shown in Fig. 1(a). This simple model can be regarded as a strained graphene lattice [44–48] which is uniaxially strained along the y direction.

We introduce the Fourier transformations,

$$(a_{\mathbf{k}}, b_{\mathbf{k}}) = \frac{1}{\sqrt{MN}}\sum_{\mathbf{r}}(a_{\mathbf{r}}, b_{\mathbf{r}})e^{-i\mathbf{k}\cdot\mathbf{r}}. \qquad (5)$$

Then, the Hamiltonian with periodic boundary conditions in both directions can be block diagonalized as

$$H = \sum_{\mathbf{k}}(a_{\mathbf{k}}^{\dagger} \quad b_{\mathbf{k}}^{\dagger})h(\mathbf{k})\begin{pmatrix}a_{\mathbf{k}} \\ b_{\mathbf{k}}\end{pmatrix}, \qquad (6)$$

with the core matrix,

$$h(\mathbf{k}) = \begin{pmatrix} 0 & g(\mathbf{k}) \\ g^*(\mathbf{k}) & 0 \end{pmatrix}, \qquad (7)$$

and $g(\mathbf{k}) = \mu + (e^{ik_x} + e^{ik_y})$. We note that the system respects time reversal, chiral, and particle-hole symmetry, i.e., for the Bloch Hamiltonian $h(\mathbf{k})$, we have $\mathcal{T}h(\mathbf{k})\mathcal{T}^{-1} = h(-\mathbf{k})$, $\mathcal{S}h(\mathbf{k})\mathcal{S}^{-1} = -h(\mathbf{k})$, and $\mathcal{C}h(\mathbf{k})\mathcal{C}^{-1} = -h(-\mathbf{k})$ with $\mathcal{T} = \mathcal{K}$ as the complex-conjugation operator, and
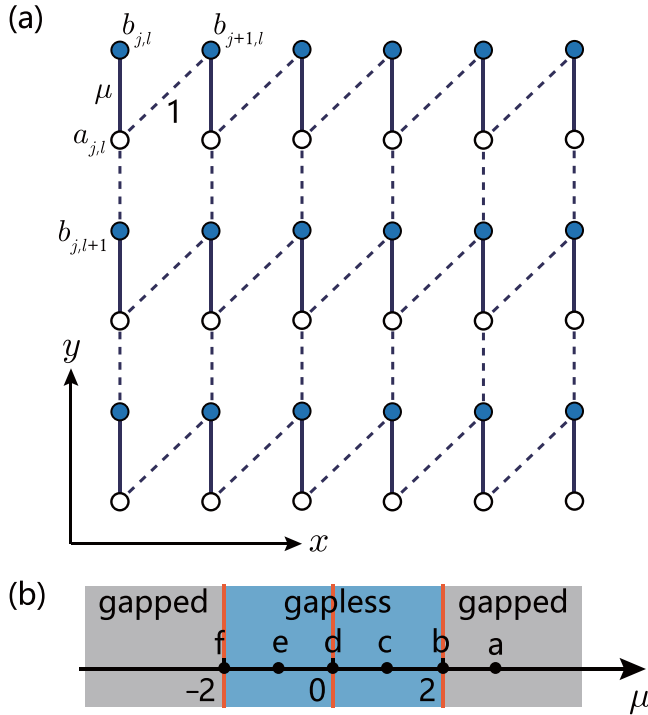
FIG. 1. (a) Schematic of the 2D tight-binding model with Hamiltonian Eq. (4), which is essentially a bipartite $M \times N$ honeycomb lattice. The solid lines and dashed lines represent hopping terms with strengths μ and 1, respectively. (b) Phase diagram of the lattice system with parameter μ. The orange lines indicate the phase boundary, which separate the topologically trivial gapped phases (gray) and topological gapless phases (blue). The system with the parameter at the boundary (orange lines) is a topologically trivial gapless phase. Points (a)–(f) represent the systems in each phase, which are extensively investigated in Fig. 3.

$\mathcal{S} = \sigma_z$, $\mathcal{C} = \sigma_z \mathcal{K}$. The core matrix can be written as

$$h(\mathbf{k}) = \mathbf{B}(\mathbf{k}) \cdot \sigma, \tag{8}$$

where the components of the Bloch vector $\mathbf{B}(\mathbf{k}) = (B_x, B_y, B_z)$ are

$$
\begin{aligned}
B_x &= \mu + (\cos k_x + \cos k_y), \\
B_y &= -(\sin k_x + \sin k_y), \\
B_z &= 0,
\end{aligned}
\tag{9}
$$

and $\sigma = (\sigma_x, \sigma_y, \sigma_z)$ are the Pauli matrices. The spectrum is

$$E_{\mathbf{k}}^{\pm} = \pm \sqrt{(\mu + \cos k_x + \cos k_y)^2 + (\sin k_x + \sin k_y)^2}. \tag{10}$$

We focus on the gapless phase arising from the band-degenerate points of the spectrum. The band-degenerate point $\mathbf{k}_0 = (k_{0x}, k_{0y})$ fulfills the equations,

$$
\begin{aligned}
\sin k_{0x} + \sin k_{0y} &= 0, \\
\mu + \cos k_{0x} + \cos k_{0y} &= 0.
\end{aligned}
\tag{11}
$$

As shown in Figs. 3(a1)–3(f1), there are three types of band-touching configurations: Single point, double points, and lines

on the k_x-k_y plane, determined by the parameter μ. We are interested in the nontrivial case (double points) with nonzero μ. Then, from Eq. (11), we have

$$k_{0x} = -k_{0y} = \pm \arccos\left(-\frac{\mu}{2}\right), \tag{12}$$

in the condition of $|\mu| \leqslant 2$. It indicates that there are two degenerate points for $\mu \neq 0$ and $|\mu| \neq 2$. When μ's vary, the two points move along the line: $k_{0x} = -k_{0y}$ and merge at $\mathbf{k}_0 = (\pm\pi, \mp\pi)$ or $\mathbf{k}_0 = (0, 0)$ when $\mu = 2$ or $\mu = -2$. In the case of $\mu = 0$, the degenerate points become two degenerate lines: $k_{0y} = \pm\pi + k_{0x}$. The phase diagram is shown in Fig. 1(b), and the bulk spectra for several typical cases are illustrated in Figs. 3(a1)–3(f1).

The gapless phase of this model can be protected by a $\mathbb{Z}$-type invariant according to the classification topological semimetals [3,49]. For the isolated band-touching point, the topological nature of the band degeneracy can be considered as a vortex in the momentum space with integer winding numbers, which is equivalent to the concept of the Berry flux [50,51]. The Berry flux is defined as the contour integral of the Berry connection in the momentum space [50,52]. A band-degenerate point can be regarded as a topological defect, and the topological index can be extracted from the expression of Bloch vector $\mathbf{B}(\mathbf{k})$. Actually, in the vicinity of the degenerate points, the Bloch vector can be expressed as the form

$$
\begin{aligned}
B_x &= -\sin k_{0x}(q_x - q_y), \\
B_y &= -\cos k_{0x}(q_x + q_y), \\
B_z &= 0,
\end{aligned}
\tag{13}
$$

where $\mathbf{q} = \mathbf{k} - \mathbf{k}_0$ is the momentum in another frame and $\mathbf{k}_0 = (k_{0x}, k_{0y})$ satisfies Eq. (12). Around these degenerate points, the core matrix $h(\mathbf{k})$ can be linearized as

$$h(\mathbf{q}) = \sum_{i,j=1}^{2} c_{ij} q_i \sigma_j, \tag{14}$$

which is equivalent to the Hamiltonian for 2D massless relativistic fermions. Here, $(q_1, q_2) = (q_x, q_y)$, $(\sigma_1, \sigma_2) = (\sigma_x, \sigma_y)$ and $c = \left(\begin{smallmatrix} -\sin k_{0x} & -\cos k_{0x} \\ \sin k_{0x} & -\cos k_{0x} \end{smallmatrix}\right)$. The corresponding chirality for these particles is defined as

$$w = \text{sgn}[\det(c)] = \text{sgn}[\sin(2k_{0x})], \tag{15}$$

which leads to $w = \pm 1$ for two degenerate points. The chiral relativistic fermions serve as 2D Dirac points. Two Dirac points located at two separated degenerate points have opposite chirality. We note that $w = 0$ for $\mu = 0$ and $|\mu| = 2$. When $\mu = -2$ or $\mu = 2$, two Dirac points merge at $(0,0)$ or $(\pm\pi, \mp\pi)$ and become a single degenerate point. The topology of the degenerate point becomes trivial, and a perturbation, hence, can open up the bulk energy gap. We illustrate the Bloch vector fields on the k_x-k_y plane for several typical cases in Figs. 3(a2)–3(f2). As shown in the figures, we find three types of topological configurations: A pair of vortices with opposite chirality, a single trivial vortex (or degeneracy lines), and no vortex, corresponding to topological gapless, trivial gapless, and gapped phases, respectively. According to the bulk-boundary correspondence [3,49], the nontrivial bulk topology would lead to the protected surface states and
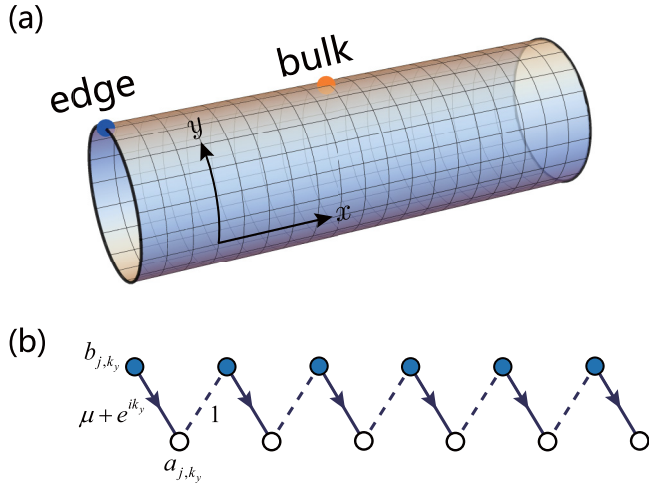
FIG. 2. (a) Schematic of the geometry of the system with the cylindrical boundary condition. The locations of the initial local states at the edge (blue dot) and bulk (orange dot) of the 2D lattice system are indicated. (b) Schematic of the modified Su-Schrieffer-Heeger (SSH) chain H_k represented in Eq. (18). The arrows and dashed lines represent complex and real hopping terms ($\mu + e^{ik}$) and 1, respectively. The edge modes of a set of modified SSH chains form the flatband edge modes as bound states located at two edges of the cylinder when the system is in the blue region of the phase diagram in Fig. 1(b).

forming the flatband when the open boundary condition is applied as we can see in the following.

B. Flatband edge modes

Now, we turn to study the feature of the gapless phase of the square lattice. At first, we revisit the description of the present model with the cylindrical boundary condition as shown in Fig. 2(a). Consider the Fourier transformations in the y direction,

$$(a_{j,k_y}, b_{j,k_y}) = \frac{1}{\sqrt{N}} \sum_{l=1}^{N} e^{-ik_y l}(a_{j,l}, b_{j,l}), \quad (16)$$

where the wave-vector $k_y = 2\pi n/N$, $n = 1, 2, \ldots, N$. The Hamiltonian H can be rewritten as

$$H = \sum_{k_y} H_{k_y}, \quad (17)$$

with

$$H_{k_y} = \sum_{j=1}^{N} \delta_{k_y} a_{j,k_y}^{\dagger} b_{j,k_y} + \sum_{j=1}^{N-1} a_{j,k_y}^{\dagger} b_{j+1,k_y} + \text{H.c.}, \quad (18)$$

where $\delta_{k_y} = (\mu + e^{ik_y})$, and H_{k_y} obeys $[H_{k_y}, H_{k_y'}] = 0$, i.e., H has been block diagonalized. We note that each H_{k_y} represents a modified SSH chain with hopping terms δ_{k_y} and 1. The schematic is shown in Fig. 2(b).

The flatband edge modes of the 2D chiral symmetric Hamiltonian Eq. (4) with the cylindrical boundary condition are originated from the zero energy edge states of the modified SSH in Eq. (18), which can be related to the winding number [28,53–56] or Zak phase [57]. The winding number for the

bulk Hamiltonian of Eq. (18) is defined as [56]

$$\mathcal{W}(k_y) = \frac{1}{2\pi i} \int_{-\pi}^{\pi} dk_x \partial_{k_x} \ln g(\mathbf{k}), \quad (19)$$

where $g(\mathbf{k})$ is an off-diagonal element of the core matrix $h(\mathbf{k})$ of the 2D bulk Hamiltonian in Eq. (6). Direct derivation gives

$$\mathcal{W}(k_y) = \begin{cases} 1, & \mu(\mu + 2\cos k_y) < 0, \\ 0, & \mu(\mu + 2\cos k_y) > 0. \end{cases} \quad (20)$$

The winding number is 1 for the parameter region $\mu(\mu + 2\cos k_y) < 0$ in which the open chain in Eq. (18) is expected to exist with 1 pair of zero energy edge states [55], respectively, localized at two ends of the chain. These zero energy edge states for all k_y's in the above parameter region form the flatband edge modes for the 2D lattice with cylindrical geometry.

One can always get a diagonalized H_{k_y} through the diagonalization of the matrix of the corresponding single-particle SSH chain. Actually, it can be checked that H_{k_y} exits two zero modes in the large-N limit,

$$|\psi_R\rangle = \Omega \sum_{j=1}^{N} \left(-\delta_{k_y}^*\right)^{N-j} a_{j,k_y}^{\dagger} |\text{vac}\rangle,$$

$$|\psi_L\rangle = \Omega \sum_{j=1}^{N} \left(-\delta_{k_y}\right)^{j-1} b_{j,k_y}^{\dagger} |\text{vac}\rangle, \quad (21)$$

where $\Omega = \sqrt{1 - |\delta_{k_y}|^2}$ is the normalization constant and $|\delta_{k_y}| < 1$ represents the edge modes localizing at the right or left of the SSH chain. The condition $|\delta_{k_y}| = |\mu + e^{ik_y}| < 1$ leads to $\mu(\mu + 2\cos k_y) < 0$, and the interval of edge modes for k_y is

$$k_y \in \mathcal{I} = \begin{cases} \left(-\pi, -k_y^c\right) \cup \left(k_y^c, \pi\right], & 0 < \mu < 2, \\ \left(-k_y^c, k_y^c\right), & -2 < \mu < 0, \end{cases} \quad (22)$$

with $k_y^c = \arccos(-\mu/2)$. The above interval $\mathcal{I}$ matches with the interval with nonzero winding number in Eq. (20). The zero modes in the plot of the energy band in Figs. 3(c3) and 3(e3) correspond this flatband of edge modes. For an arbitrary site-state $a_{N,j}^{\dagger} |\text{vac}\rangle$ (or $b_{1,j}^{\dagger} |\text{vac}\rangle$) at the edge, the total probability of the component of edge state $|\psi_R\rangle$ (or $|\psi_L\rangle$) is

$$p = \frac{1}{N} \sum_{k_y \in \mathcal{I}} \left(1 - |\delta_{k_y}|^2\right) \approx \frac{1}{2\pi} \int_{\mathcal{I}} \left(1 - |\delta_{k_y}|^2\right) dk_y, \quad (23)$$

which is only μ dependent in the large-N limit. We will see that p can be measured by the LE of the edge site state.

IV. DYNAMIC DETECTION OF EDGE MODES

In this section, we focus on the dynamics of the system in the presence of disorder. As we know, one of the most striking features of topologically protected edge states is the robustness against certain types of disordered perturbation to the original Hamiltonian. The disorder we discuss here arises from the hopping integrals in the Hamiltonian H from Eq. (4) with the cylindrical boundary condition. In the presence of
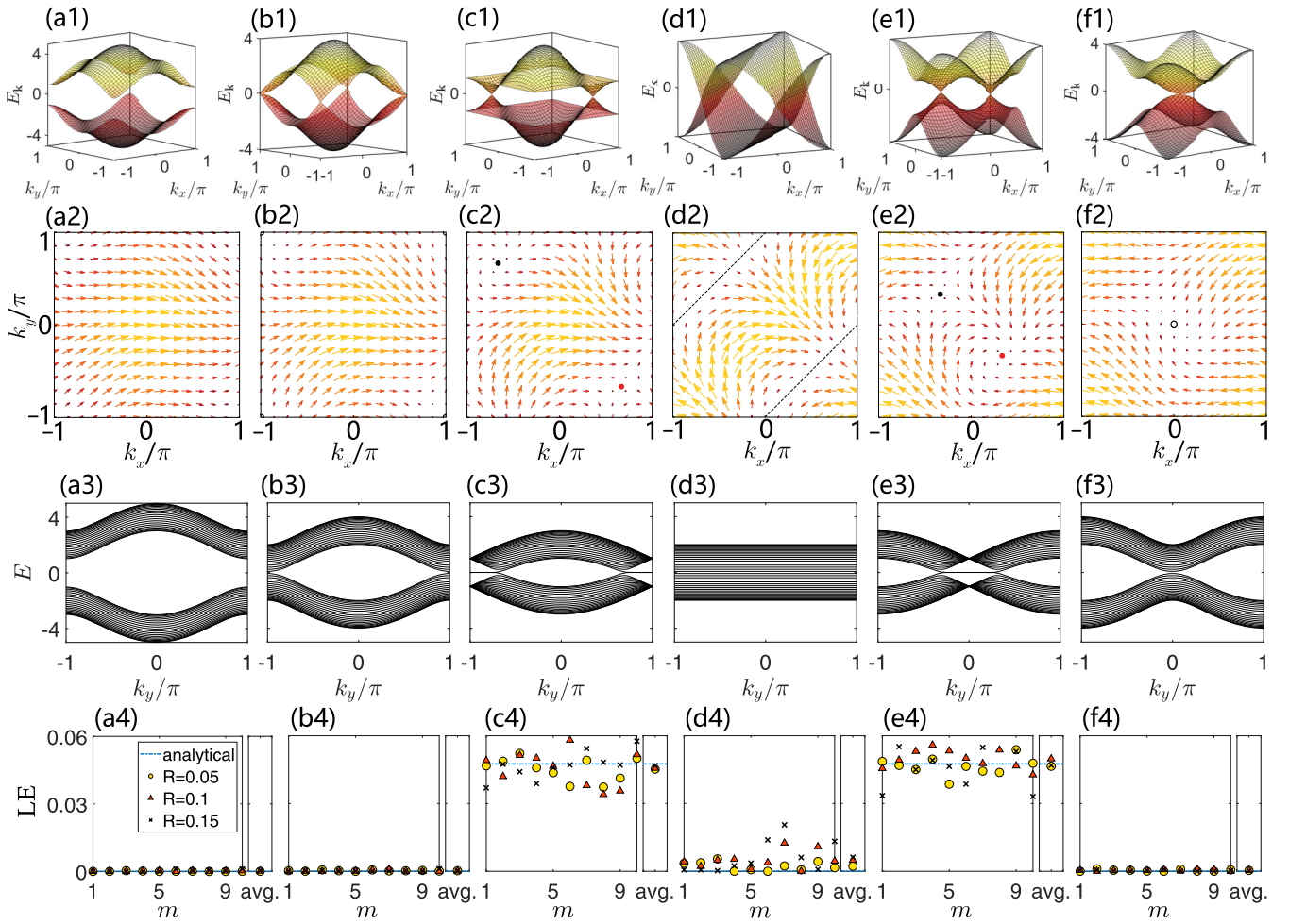
FIG. 3. Kaleidoscope of quantum phases. (a1)–(f1) Plots of energy spectra from Eq. (10) at six typical points (a–f) marked in the phase diagram in Fig. 1(b). There, the band structure exhibits a bulk gap in (a1); a single degeneracy point with parabolic dispersion in (b1) and (f1); two degeneracy points with linear dispersion in (c1) and (e1); and two degeneracy lines in (d1). (a2)–(f2) Plots of the Bloch vector field defined in Eq. (9) in the momentum space for six cases corresponding to (a1)–(f1). There are two vortices in (c2) and (e2) with opposite winding numbers ±1. As μ increases or decreases, two vortices get close and merge into a single point in (b2) or (f2), and disappear in (a2). (a3)–(f3) Plots of the spectra of a set of modified SSH chains [Eq. (17)] in open boundary condition with $N = 40$ for six cases corresponding to (a1)–(f1). It indicates that the existence of pair of vortices links to a flatband of the square lattice. (a4)–(f4) Plots of the LE obtained by numerical simulations from Eq. (1) at $t = 3000J^{-1}$ and analytical expressions from Eq. (28) in which the initial state is taken as the site state at the edge. Here, J is the scale of the Hamiltonian, and we take $J = 1$. R is the disorder strength, and m denotes the measurement index. The average value of the LEs are plotted on the right of each panel. The size of the system is $M \times N = 80 \times 80$.

disorder, the Hamiltonian reads

$$H_D = \sum_{\mathbf{r}} (\mu_{\mathbf{r}} a_{\mathbf{r}}^\dagger b_{\mathbf{r}} + \nu_{\mathbf{r}} a_{\mathbf{r}}^\dagger b_{\mathbf{r}+\hat{x}} + \lambda_{\mathbf{r}} a_{\mathbf{r}}^\dagger b_{\mathbf{r}+\hat{y}}) + \text{H.c.}, \quad (24)$$

where parameters $\{\mu_{\mathbf{r}}, \nu_{\mathbf{r}}, \lambda_{\mathbf{r}}\}$ are three sets of position-dependent numbers. Here, we take

$$\begin{aligned} \mu_{\mathbf{r}} &= \mu + d_{\mu,\mathbf{r}}, \\ \nu_{\mathbf{r}} &= 1 + d_{\nu,\mathbf{r}}, \quad (25) \\ \lambda_{\mathbf{r}} &= 1 + d_{\lambda,\mathbf{r}}, \end{aligned}$$

where $d_{\mu,\mathbf{r}}$, $d_{\nu,\mathbf{r}}$, and $d_{\lambda,\mathbf{r}}$ are uniform random real numbers within the interval $[-R, R]$, taking the role of the disorder strength, and $\mathbf{r}$ is the site index.

Now, we investigate the influence of nonzero R by comparing two sets of eigenvalues obtained by numerical

diagonalization of finite-dimensional matrices of H and H_D in single-particle subspace, respectively. The plots in Fig. 4 indicate that the zero modes remain unchanged in the presence of chiral-symmetry-preserving random perturbations with not too large R. The chiral symmetry, here, is responsible for the existence of zero modes, in other words, under chiral-symmetry-breaking disordered perturbation, the zero modes no longer survive. Taking the disordered on-site potential, for example, the Hamiltonian reads $H' = H + \sum_{\mathbf{r}} (d_{a,\mathbf{r}} a_{\mathbf{r}}^\dagger a_{\mathbf{r}} + d_{b,\mathbf{r}} b_{\mathbf{r}}^\dagger b_{\mathbf{r}})$, where $d_{a,\mathbf{r}}$ and $d_{b,\mathbf{r}}$ are uniform random real numbers within the interval $[-R, R]$. The numerical results in Fig. 4 indicate that, under this kind of chiral-symmetry-breaking disordered perturbation, the zero modes do not survive, which may lead to the decay of the LE in contrast to Eqs. (2) and (3), although the original edge states remain localized on the edge. Furthermore, we
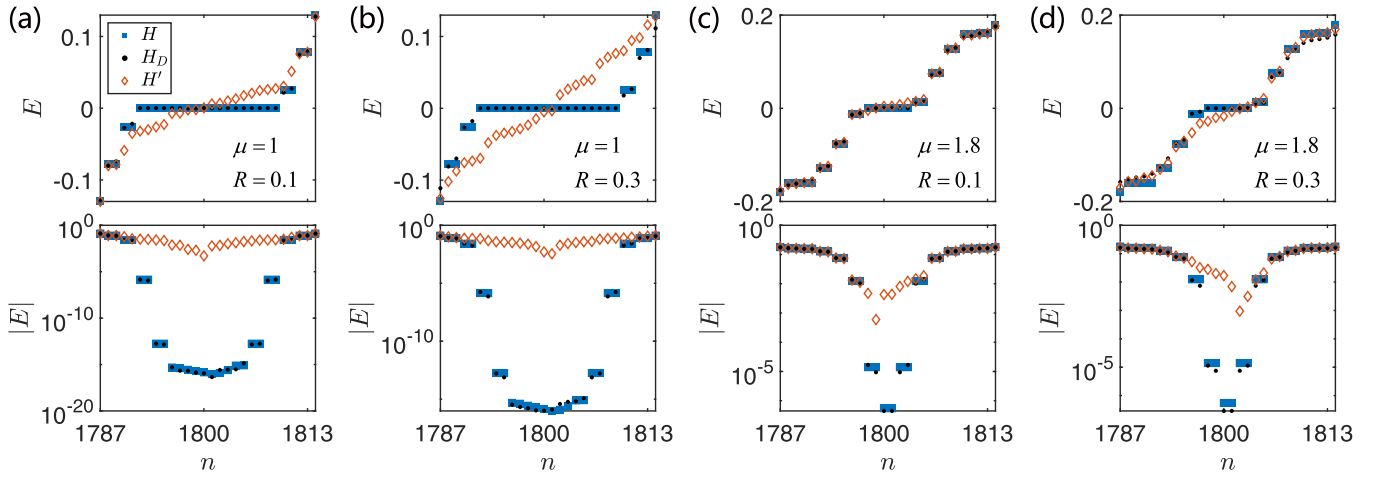
FIG. 4. Linear and logarithmic scale plots of eigenenergy around zero for H, H_D, and H' with the cylindrical boundary condition. n denotes the sorting index. The parameters are $\mu = 1$ for (a) and (b); $\mu = 1.8$ for (c) and (d); $R = 0.1$ for (a) and (c); $R = 0.3$ for (b) and (d). It indicates that the number of zero modes is dependent on μ, and the zero modes remain unchanged in the presence of the chiral-symmetry-preserving disordered perturbation whereas they do not survive under the chiral-symmetry-breaking disordered perturbation. The results are obtained by numerical diagonalization for the system with $M \times N = 60 \times 60$.

investigate the IPR for the gapless phase with and without chiral-symmetry-preserving disorder. The IPR is defined as $\mathrm{IPR}(E) = \sum_{\mathbf{r}} |\langle \mathbf{r}|\psi_E\rangle|^4$ with E denoting the energy levels and $\mathbf{r}$ denoting the lattice sites. The numerical results of IPR shown in Fig. 5 indicate that all the states with energy $E \neq 0$
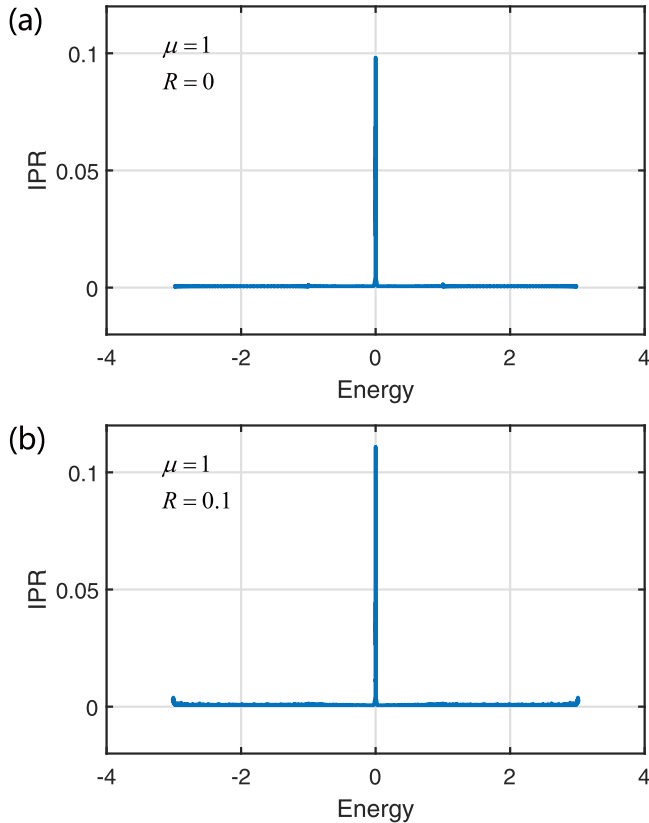

FIG. 5. Numerical results of inverse participation ratio (IPR) for the gapless phase with $\mu = 1$ corresponding to Fig. 4(a). (a) System without disorder. (b) System with chiral-symmetry-preserving disorder $R = 0.1$. The size of the system is $M \times N = 60 \times 60$.

are extended in the presence or absence of weak disorder, and the system is gapless in the transport sense.

According to the analysis in Sec. II, the LEs should have diametrically opposite behaviors for the initial bulk and edge states, respectively. To verify this point, we compute the LEs for two initial states: (i) a Gaussian wave packet in the bulk $|\psi_G\rangle$ and (ii) an edge state $|\psi_R\rangle$ or $|\psi_L\rangle$. In Fig. 6, we plot the result, which is in agreement with our prediction. We find that, when $|\psi(0)\rangle$ is a bulk state, $M(t)$ will decay exponentially, whereas $M(t)$ remains in the constant 1 when $|\psi(0)\rangle = |\psi_R\rangle$ or $|\psi_L\rangle$. Accordingly, when we take the initial state as the superposition of scattering and bound states, i.e.,

$$|\psi(0)\rangle = c_G|\psi_G\rangle + c_R|\psi_R\rangle + c_L|\psi_L\rangle, \quad (26)$$

with $|c_G|^2 + |c_R|^2 + |c_L|^2 = 1$, we can have the LE after a long time,

$$\lim_{t\to\infty} M(t) = |c_R|^2 + |c_L|^2 = 1 - |c_G|^2. \quad (27)$$

It indicates that the magnitude of c_G can be measured by the LE. Furthermore, if we take $|\psi(0)\rangle = a_{N,j}^{\dagger}|\mathrm{vac}\rangle$ (or $b_{1,j}^{\dagger}|\mathrm{vac}\rangle$), the population of survival zero modes is a function of μ, which also relates to the quantity p, i.e.,

$$\lim_{t\to\infty} M(t) = \lim_{t\to\infty} |\langle\psi(0)|e^{iH_D t}e^{-iH_0 t}|\psi(0)\rangle|^2 \approx p^2 \quad (28)$$

for the very weak disordered system H_D. It is presumable that the size of flatband k_c can be obtained by the LE in the dynamical process.

To demonstrate and verify this scheme, we perform numerical simulations. We choose three different strengths of chiral-symmetry-preserving disorder R and six typical values of hopping amplitudes μ. The numerical simulations are performed ten times for each set of the parameter. Figures 3(a4)–3(f4) plot the convergent LEs, where $\mathrm{LE} = \lim_{t\to\infty} M(t)$ is obtained by taking a sufficiently large t ($t = 3000$) for several typical μ's with different strengths of chiral-symmetry-preserving disorder $R = 0.04$, 0.1 and 0.15. It indicates that a single measurement result depends on the setting random
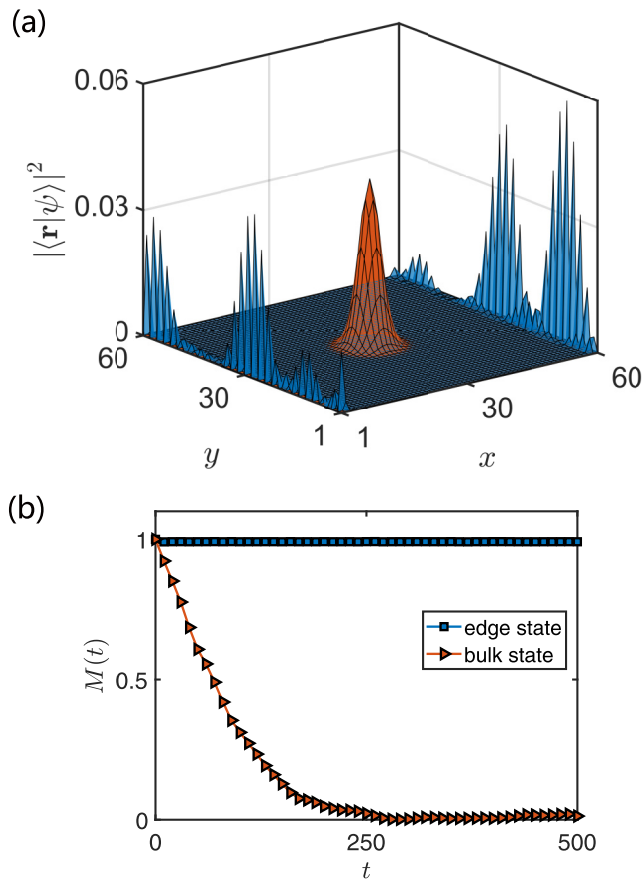
(a)

(b)

FIG. 6. (a) Profiles of the initial states of numerical simulations for the LEs. The edge state (blue) is taken as the eigenstate of system in the cylindrical boundary condition without disorder, and the bulk state (orange) is taken as the 2D Gaussian wave packet. (b) Plots of numerical simulations for the LEs as the functions of time. The initial states are taken as the edge state and bulk state shown in (a). It can be seen that the LEs have diametrically opposite behaviors for the initial bulk and edge states. The time t is in units of J^{-1}, where J is the scale of the Hamiltonian, and we take $J = 1$. The size of the system is $M \times N = 60 \times 60$, and the disorder strength is $R = 0.1$.

number. The average of multimeasurement result $\langle \text{LE} \rangle$ is very close to the analytical result in the blue dashed lines. The dependence of $\langle \text{LE} \rangle$ on μ for a wide range of μ with the disorder strength $R = 0.1$ are presented in Fig. 7. The comparison between analytical and numerical results shows that the LE method has good accuracy to determine the positions of vortices as well as the phase diagram. The transition points occur at $\mu = \pm 2$, associated with the vanishing $\langle \text{LE} \rangle$.
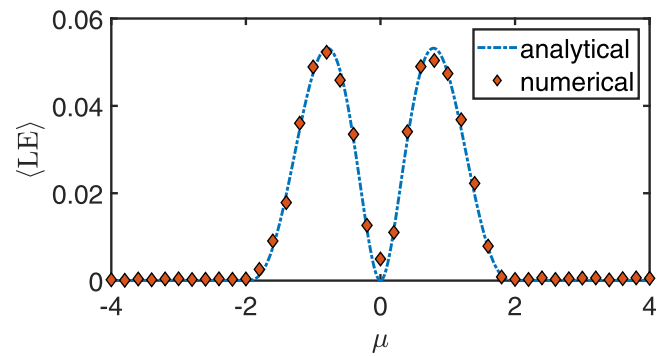

FIG. 7. Comparison of the average convergent LEs and analytical expression from Eq. (28) as the functions of μ. The initial state is a edge site state, and the final time is $t = 1000J^{-1}$, where J is the scale of the Hamiltonian, and we take $J = 1$. The size of the system is $M \times N = 60 \times 60$, and the disorder strength is $R = 0.1$. It is found that the two results agree with each other well. This means that the measurement of the LE can identify the phase diagram.

The data and codes of the numerical calculations of Figs. 3–7 are available in the Supplemental Material as well as in ZENODO [58].

V. DISCUSSION

In this paper, we have proposed a way to detect the positions of two vortices in 2D momentum space as well as the phase diagram. The advantage of this scheme is not limited by the imperfection of the system, but in the aid of the disorder. The photonic system is a candidate for the realization of the scheme in experiment, beyond the solid-state electron systems. The field of topological photonics grows rapidly and aims to explore the physics of topological phases of matter in the context of optics. Photonic systems provide a natural and convenient medium to investigate fundamental quantum transport properties. Using photons, one can selectively excite a site state and observe the spatial responses throughout the material, which are challenging tasks in electronic systems. Recently, it has been shown that the Loschmidt echo of photons can be observed in a binary waveguide by exchanging the two sublattices after some propagation distance [59]. The dynamic feature of topological edge states and the phase diagram presented in this paper potentially can be utilized for developing inherently robust artificial photonic devices.

[1] M. Z. Hasan and C. L. Kane, *Colloquium*: Topological insulators, Rev. Mod. Phys. **82**, 3045 (2010).

[2] X. L. Qi and S. C. Zhang, Topological insulators and superconductors, Rev. Mod. Phys. **83**, 1057 (2011).

[3] C. K. Chiu, J. C. Y. Teo, A. P. Schnyder, and S. Ryu, Classification of topological quantum matter with symmetries, Rev. Mod. Phys. **88**, 035005 (2016).

[4] H. Weng, R. Yu, X. Hu, X. Dai, and Z. Fang, Quantum anomalous Hall effect and related topological electronic states, Adv. Phys. **64**, 227 (2015).

[5] L. Fu and C. L. Kane, Superconducting Proximity Effect and Majorana Fermions at the Surface of a Topological Insulator, Phys. Rev. Lett. **100**, 096407 (2008).

[6] R. M. Lutchyn, J. D. Sau, and Sarma, Majorana Fermions and a Topological Phase Transition in Semiconductor-Superconductor Heterostructures, Phys. Rev. Lett. **105**, 077001 (2010).

[7] V. Mourik, K. Zuo, S. M. Frolov, S. R. Plissard, E. P. A. M. Bakkers, and L. P. Kouwenhoven, Signatures of Majorana Fermions in Hybrid Superconductor-Semiconductor Nanowire Devices, Science **336**, 1003 (2012).

[8] S. Nadj-Perge, I. K. Drozdov, J. Li, H. Chen, S. Jeon, J. Seo, A. H. MacDonald, B. A. Bernevig, and A. Yazdani, Observation of Majorana fermions in ferromagnetic atomic chains on a superconductor, Science **346**, 602 (2014).

[9] Y. Oreg, G. Refael, and F. von Oppen, Helical Liquids and Majorana Bound States in Quantum Wires, Phys. Rev. Lett. **105**, 177002 (2010).

[10] N. Read and D. Green, Paired states of fermions in two dimensions with breaking of parity and time-reversal symmetries and the fractional quantum Hall effect, Phys. Rev. B **61**, 10267 (2000).

[11] A. H. C. Neto, F. Guinea, N. M. R. Peres, K. S. Novoselov, and A. K. Geim, The electronic properties of graphene, Rev. Mod. Phys. **81**, 109 (2009).

[12] Z. K. Liu, J. Jiang, B. Zhou, Z. J. Wang, Y. Zhang, H. M. Weng, D. Prabhakaran, S-K. Mo, H. Peng, P. Dudin, T. Kim, M. Hoesch, Z. Fang, X. Dai, Z. X. Shen, D. L. Feng, Z. Hussain, and Y. L. Chen, A stable three-dimensional topological Dirac semimetal Cd_3As_2, Nat. Mater. **13**, 677 (2014).

[13] Z. K. Liu, B. Zhou, Y. Zhang, Z. J. Wang, H. M. Weng, D. Prabhakaran, S.-K. Mo, Z. X. Shen, Z. Fang, X. Dai, Z. Hussain, and Y. L. Chen, Discovery of a Three-Dimensional Topological Dirac Semimetal, Na_3Bi, Science **343**, 864 (2014).

[14] J. A. Steinberg, S. M. Young, S. Zaheer, C. L. Kane, E. J. Mele, and A. M. Rappe, Bulk Dirac Points in Distorted Spinels, Phys. Rev. Lett. **112**, 036403 (2014).

[15] Z. Wang, Y. Sun, X.-Q. Chen, C. Franchini, G. Xu, H. Weng, X. Dai, and Z. Fang, Dirac semimetal and topological phase transitions in A_3Bi(A=Na, K, Rb), Phys. Rev. B **85**, 195320 (2012).

[16] J. Xiong, S. K. Kushwaha, T. Liang, J. W. Krizan, M. Hirschberger, W. Wang, R. J. Cava, and N. P. Ong, Evidence for the chiral anomaly in the dirac semimetal Na_3Bi, Science **350**, 413 (2015).

[17] S. M. Young, S. Zaheer, J. C. Y. Teo, C. L. Kane, E. J. Mele, and A. M. Rappe, Dirac Semimetal in Three Dimensions, Phys. Rev. Lett. **108**, 140405 (2012).

[18] M. Hirschberger, S. Kushwaha, Z. Wang, Q. Gibson, S. Liang, C. A. Belvin, B. A. Bernevig, R. J. Cava, and N. P. Ong, The chiral anomaly and thermopower of Weyl fermions in the half-Heusler GdPtBi, Nat. Mater. **15**, 1161 (2016).

[19] S.-M. Huang, S.-Y. Xu, I. Belopolski, C.-C. Lee, G. Chang, B. Wang, N. Alidoust, G. Bian, M. Neupane, C. Zhang, S. Jia, A. Bansil, H. Lin, and M. Z. Hasan, A Weyl Fermion semimetal with surface Fermi arcs in the transition metal monopnictide TaAs class, Nat. Commun. **6**, 7373 (2015).

[20] B. Q. Lv, H. M. Weng, B. B. Fu, X. P. Wang, H. Miao, J. Ma, P. Richard, X. C. Huang, L. X. Zhao, G. F. Chen, Z. Fang, X. Dai, T. Qian, and H. Ding, Experimental Discovery of Weyl Semimetal TaAs, Phys. Rev. X **5**, 031013 (2015).

[21] B. Q. Lv, N. Xu, H. M. Weng, J. Z. Ma, P. Richard, X. C. Huang, L. X. Zhao, G. F. Chen, C. E. Matt, F. Bisti, V. N. Strocov, J. Mesot, Z. Fang, X. Dai, T. Qian, M. Shi, and H. Ding, Observation of Weyl nodes in TaAs, Nat. Phys. **11**, 724 (2015).

[22] C. Shekhar, N. Kumar, V. Grinenko, S. Singh, R. Sarkar, H. Luetkens, S.-C. Wu, Y. Zhang, A. C. Komarek, E. Kampert, Y. Skourski, J. Wosnitza, W. Schnelle, A. McCollam, U. Zeitler, J. Kübler, B. Yan, H.-H. Klauss, S. S. P. Parkin, and C. Felser, Anomalous Hall effect in Weyl semimetal half-Heusler compounds RPtBi (R = Gd and Nd), Proc. Natl. Acad. Sci. USA **115**, 9140 (2018).

[23] X. Wan, A. M. Turner, A. Vishwanath, and S. Y. Savrasov, Topological semimetal and Fermi-arc surface states in the electronic structure of pyrochlore iridates, Phys. Rev. B **83**, 205101 (2011).

[24] H. Weng, C. Fang, Z. Fang, B. A. Bernevig, and X. Dai, Weyl Semimetal Phase in Noncentrosymmetric Transition-Metal Monophosphides, Phys. Rev. X **5**, 011029 (2015).

[25] S.-Y. Xu, N. Alidoust, I. Belopolski, Z. Yuan, G. Bian, T.-R. Chang, H. Zheng, V. N. Strocov, D. S. Sanchez, G. Chang, C. Zhang, D. Mou, Y. Wu, L. Huang, C.-C. Lee, S.-M. Huang, B. Wang, A. Bansil, H.-T. Jeng, T. Neupert, A. Kaminski, H. Lin, S. Jia, and M. Z. Hasan, Discovery of a Weyl fermion state with Fermi arcs in niobium arsenide, Nat. Phys. **11**, 748 (2015).

[26] S.-Y. Xu, I. Belopolski, N. Alidoust, M. Neupane, G. Bian, C. Zhang, R. Sankar, G. Chang, Z. Yuan, C.-C. Lee, S.-M. Huang, H. Zheng, J. Ma, D. S. Sanchez, B. Wang, A. Bansil, F. Chou, P. P. Shibayev, H. Lin, S. Jia, and M. Z. Hasan, Discovery of a Weyl fermion semimetal and topological Fermi arcs, Science **349**, 613 (2015).

[27] M. Fujita, K. Wakabayashi, K. Nakada, and K. Kusakabe, Peculiar Localized State at Zigzag Graphite Edge, J. Phys. Soc. Jpn. **65**, 1920 (1996).

[28] S. Ryu and Y. Hatsugai, Topological Origin of Zero-Energy Edge States in Particle-Hole Symmetric Systems, Phys. Rev. Lett. **89**, 077002 (2002).

[29] W. Yao, S. A. Yang, and Q. Niu, Edge States in Graphene: From Gapped Flat-Band to Gapless Chiral Modes, Phys. Rev. Lett. **102**, 096801 (2009).

[30] K. Wakabayashi, Y. Takane, and M. Sigrist, Perfectly Conducting Channel and Universality Crossover in Disordered Graphene Nanoribbons, Phys. Rev. Lett. **99**, 036601 (2007).

[31] Z. B. Yan, R. Bi, and Z. Wang, Majorana Zero Modes Protected by a Hopf Invariant in Topologically Trivial Superconductors, Phys. Rev. Lett. **118**, 147003 (2017).

[32] Z. B. Yan, F. Song, and Z. Wang, Majorana Corner Modes in a High-Temperature Platform, Phys. Rev. Lett. **121**, 096803 (2018).

[33] Q. Y. Wang, C. C. Liu, Y. M. Lu, and F. Zhang, High-Temperature Majorana Corner States, Phys. Rev. Lett. **121**, 186801 (2018).

[34] T. Ozawa, H. M. Price, A. Amo, N. Goldman, M. Hafezi, L. Lu, M. C. Rechtsman, D. Schuster, J. Simon, O. Zilberberg, and I. Carusotto. Topological photonics, Rev. Mod. Phys. **91**, 015006 (2019).

[35] L. Lu, J. D. Joannopoulos, and M. Soljačić, Topological photonics, Nat. Photon. **8**, 821 (2014).

[36] P. W. Anderson, Absence of diffusion in certain random lattices, Phys. Rev. **109**, 1492 (1958).

[37] A. A. Chabanov, M. Stoytchev, and A. Z. Genack, Statistical signatures of photon localization, Nature (London) **404**, 850 (2000).

[38] T. Schwartz, G. Bartal, S. Fishman, and M. Segev, Transport and Anderson localization in disordered two-dimensional photonic lattices, Nature (London) **446**, 52 (2007).

[39] H. Hu, A. Strybulevych, J. H. Page, S. E. Skipetrov, and B. A. van Tiggelen, Localization of ultrasound in a three-dimensional elastic network, Nat. Phys. **4**, 945 (2008).

[40] A. P. Schnyder and S. Ryu, Topological phases and surface flat bands in superconductors without inversion symmetry, Phys. Rev. B **84**, 060504(R) (2011).

[41] A. P. Schnyder, P. M. R. Brydon, and C. Timm, Types of topological surface states in nodal noncentrosymmetric superconductors, Phys. Rev. B **85**, 024522 (2012).

[42] K. L. Zhang, P. Wang, and Z. Song, Majorana flat band edge modes of topological gapless phase in 2D Kitaev square lattice, Sci. Rep. **9**, 4978 (2019).

[43] P. Wang, S. Lin, G. Zhang, and Z. Song, Topological gapless phase in Kitaev model on square lattice, Sci. Rep. **7**, 17179 (2017).

[44] V. M. Pereira, A. H. C. Neto, and N. M. R. Peres, Tight-binding approach to uniaxial strain in graphene, Phys. Rev. B **80**, 045401 (2009).

[45] H. Rostami and R. Asgari, Electronic ground-state properties of strained graphene, Phys. Rev. B **86**, 155435 (2012).

[46] H. H. Pu, S. H. Rhim, C. J. Hirschmugl, M. Gajdardziska-Josifovska, M. Weinert, and J. H. Chen, Strain-induced bandgap engineering of graphene monoxide and its effect on graphene, Phys. Rev. B **87**, 085417 (2013).

[47] A. Sharma, V. N. Kotov, and A. H. C. Neto, Effect of uniaxial strain on ferromagnetic instability and formation of localized magnetic states on adatoms in graphene, Phys. Rev. B **87**, 155431 (2013).

[48] D. A. Bahamon and V. M. Pereira, Conductance across strain junctions in graphene nanoribbons, Phys. Rev. B **88**, 195416 (2013).

[49] C.-K. Chiu and A. P. Schnyder, Classification of reflection-symmetry-protected topological semimetals and nodal superconductors, Phys. Rev. B **90**, 205136 (2014).

[50] F. D. M. Haldane, Berry Curvature on the Fermi Surface: Anomalous Hall Effect as a Topological Fermi-Liquid Property, Phys. Rev. Lett. **93**, 206602 (2004).

[51] K. Sun, W. V. Liu, A. Hemmerich, and S. D. Sarma, Topological semimetal in a fermionic optical lattice, Nat. Phys. **8**, 67 (2012).

[52] E. I. Blount, *Solid State Physics*, edited by F. Seitz and D. Turnbull (Academic, New York, 1962), Vol. 13.

[53] S. Matsuura, P.-Y. Chang, A. P Schnyder, and S. Ryu, Protected boundary states in gapless topological phases, New J. Phys. **15**, 065001 (2013).

[54] C. L. M. Wong, J. Liu, K. T. Law, and P. A. Lee, Majorana flat bands and unidirectional Majorana edge states in gapless topological superconductors, Phys. Rev. B **88**, 060504(R) (2013).

[55] M. Milićević, T. Ozawa, G. Montambaux, I. Carusotto, E. Galopin, A. Lemaître, L. Le Gratiet, I. Sagnes, J. Bloch, and A. Amo, Orbital Edge States in a Photonic Honeycomb Lattice, Phys. Rev. Lett. **118**, 107403 (2017).

[56] J. K. Asbóth, L. Oroszlány, and A. Pályi, *A Short Course on Topological Insulators: Band Structure and Edge States in One and Two Dimensions*, Lecture Notes in Physics (Springer, Switzerland, 2016).

[57] P. Delplace, D. Ullmo, and G. Montambaux, Zak phase and the existence of edge states in graphene, Phys. Rev. B **84**, 195452 (2011).

[58] See Supplemental Material at http://link.aps.org/supplemental/10.1103/PhysRevB.101.014303 for data and codes of the numerical calculations of Figs. 3–7, or ZENODO [http://doi.org/10.5281/zenodo.3403408].

[59] S. Longhi, Photonic Loschmidt echo in binary waveguide lattices, Opt. Lett. **42**, 2551 (2017).